# On the Likelihood of Tropical–Extratropical Cloud Bands in the South Indian Convergence Zone during ENSO Events

NEIL C. G. HART AND RICHARD WASHINGTON

*School of Geography and the Environment, University of Oxford, Oxford, United Kingdom*

CHRIS J. C. REASON

*Department of Oceanography, University of Cape Town, Cape Town, South Africa*

(Manuscript received 3 April 2017, in final form 23 December 2017)

## ABSTRACT

The Southern Hemisphere subtropical convergence zones are important regions of rainfall in the subtropics. The south Indian Ocean convergence zone (SICZ) has the strongest seasonality and exhibits substantial interannual variability in strength and position during austral summer. On synoptic time scales, the SICZ is a preferred region for the formation of tropical–extratropical (TE) cloud bands with local maxima over the southern African mainland and Madagascar. This study investigates how the seasonality in satellite-observed cloud band frequency emerges from the interplay between the asynchronous seasonal cycles in convective instability and upper-level flow, as represented by reanalysis data. These atmospheric mean states are diagnosed with a gross convective instability metric and a method to distinguish between subtropical and eddy-driven jet axes. Month-by-month analysis of these diagnostics elucidates how mean-state perturbations during ENSO events modify cloud band likelihood. Typically, 150%–200% more cloud bands develop during La Niña seasons supported by 5°–10° latitudinal separation between the local subtropical and eddy-driven jets and higher values of convective instability, especially in semiarid parts of mainland southern Africa. During El Niño events, fewer cloud bands develop over southern Africa in a more convectively stable environment without a distinct subtropical jet. However, east of Madagascar cloud bands are 150% more likely. Plausible teleconnection pathways based on these ENSO-related perturbations are discussed. The paper concludes with a conceptual framing of the seasonal cycle in the mean-state pertinent to TE cloud band likelihood.

## 1. Introduction

The subtropical convergence zones provide a defining departure from zonal symmetry in the Southern Hemisphere subtropics. The South Pacific, South Atlantic, and south Indian convergence zones (SPCZ, SACZ, and SICZ, respectively) are associated with the main rainfall regions in the dry subtropical belt. People living near these regions depend on these convergences zones for rain-fed agriculture and water resources (e.g., Nogues-Paegle and Mo 1997; Griffiths et al. 2003; Usman and Reason 2004). Thus, interannual-to-interdecadal variability and climate change in these convergence zones remain important research topics. This study aims to contribute to clearer understanding of the regional climate processes associated with the seasonal cycle and its perturbation over southern Africa. Such understanding is essential for diagnosing and addressing current weaknesses in seasonal forecast models, and for assessing confidence in the regional climates produced by GCMs.

Of the three convergence zones, the SICZ is the least pronounced and only obvious in austral summer. The seasonal mean rainfall in the SICZ is characterized by synoptic tropical–extratropical (TE) interactions (Harrison 1984; Hart et al. 2013). Known regionally as tropical-temperate troughs (TTTs), these interactions produce northwest–southeast TE cloud bands on the

---

Denotes content that is immediately available upon publication as open access.

*Corresponding author*: Neil C. G. Hart, neil.hart@ouce.ox.ac.uk

DOI: 10.1175/JCLI-D-17-0221.1

leading edge of upper-tropospheric waves (Harangozo and Harrison 1983; Lindesay and Jury 1991; Todd and Washington 1999). As with TE interactions in the other Southern Hemisphere convergence zones (Streten 1973; van der Wiel et al. 2015), these cloud bands require the presence of low-latitude upper-tropospheric waves and sufficient lower-tropospheric instability for convection to initiate (Macron et al. 2014).

Interannual variability of the SICZ, in both strength and position, has been strongly linked to El Niño–Southern Oscillation (ENSO) variability. The fundamental result of Lindesay (1988) was that an eastward shift of tropical convection into the central Indian Ocean is accompanied by a northeastward displacement of the SICZ during El Niño events. This is the prevailing understanding with confirmatory results from Cook (2000) and Fauchereau et al. (2009). Cook (2001) argued that the ENSO-induced tropical Pacific SST anomalies are communicated to southern Africa and the south Indian Ocean by an atmospheric wave response, resulting in adjustments to the local Walker circulation, as suggested by Lindesay (1988). Nicholson and Kim (1997) considered that the ENSO signal was primarily mediated by modified Indian Ocean SST with associated rainfall impacts over southern Africa. Strong influence of regional SST anomalies has been demonstrated (Mason 1995; Reason et al. 2000; Rouault et al. 2003; Reason and Jagadheesha 2005), indicating that the teleconnection may involve both a direct atmospheric bridge and indirect effects through regional SST anomalies. Given that the SICZ is situated in the subtropics the influence of extratropical wave trains forced from the tropical Pacific convective anomalies is also plausible (e.g., Hoskins and Karoly 1981; Sardeshmukh and Hoskins 1988; Colberg et al. 2004).

Diagnosis of the synoptic-scale impact of these teleconnections within the SICZ has received limited attention. Research to date has primarily focused on the statistical associations between event frequency and large-scale modes of variability such as ENSO (Fauchereau et al. 2009; Manhique et al. 2011; Ratna et al. 2013).

ENSO-related perturbations to the seasonal cycle of southern African cloud bands remain undiagnosed as does the seasonal cycle in the mean-state thermodynamics and circulation, which support TE interactions in the SICZ. There is, however, good precedent to consider the seasonal progression of circulation. The seasonal cycle in TE cloud bands over southern Africa and the southwest Indian Ocean is pronounced (Hart et al. 2013) and the development of ENSO events is phased locked to the seasonal cycle in tropical Pacific SST (e.g., Rasmusson and Carpenter 1982; Tziperman et al. 1994) as are the regional anomalies in air–sea interactions (Hermes and Reason 2005; Ratnam et al. 2015).

The aim of this study is to address these gaps in the literature, guided by three questions:

1) What is the change in the seasonal cycle of TE cloud band likelihood during ENSO events?
2) What seasonal adjustments to the large-scale tropical and extratropical atmosphere accompany the formation of TE cloud bands and how is this modulated by ENSO?
3) Do large-scale mean-state circulation changes impact the synoptic-scale diagnostics of the TE cloud bands that do develop or do they only influence the likelihood of development?

We will demonstrate that by considering the seasonal cycle month by month, we are able to develop a conceptual framing of interannual variability in SICZ that can better account for the inter-ENSO variability in the southern African regional response. The regional processes that can enhance or diminish the ENSO signal over southern Africa are discussed more fully in the next section.

## 2. Modulation of the ENSO impact over southern Africa

The projection of ENSO into the seasonal cycle over southern Africa, as it evolves month by month, has received almost no attention to date. Similarly, very little research exists on the detailed structure of the upper-level westerly flow in the subtropical South Atlantic to south Indian sector. This section provides a conceptual framing by drawing on important literature that point to these two gaps in current understanding. We first consider the impact of ENSO on the conditions favoring rainfall over southern Africa.

Studies of ENSO impact on southern African rainfall have primarily focused on accumulated summer season rainfall anomalies. Lindesay (1988) demonstrated the dominant effect ENSO variability had on January–February–March (JFM) anomalies. However, the strength of this impact has varied in the observational record (Richard et al. 2000). This is potentially due to inter-event diversity of ENSO SST anomalies (e.g., Reason and Jagadheesha 2005; Ratnam et al. 2014). Hoell et al. (2015) showed that differences in the Indian Ocean SST response to the diverse Pacific SST expressions of El Niño events since 1950 were important in determining the regional rainfall deficits. It is widely acknowledged that part of the variation in the ENSO response is due to the modulating impact of regional SST anomalies in the South Atlantic (Rouault et al. 2003; Colberg et al. 2004; Reason and Jagadheesha 2005;

Hermes and Reason 2009), the Agulhas Current region south of the subcontinent (Reason and Mulenga 1999), and the subtropical south Indian Ocean (Nicholson and Kim 1997; Landman and Mason 1999; Reason et al. 2000).

Behera and Yamagata (2001) described a subtropical Indian Ocean dipole (SIOD) mode that was associated with changes in moisture transport toward southern Africa. Reason and Mulenga (1999), Reason (2001, 2002), and Washington and Preston (2006) demonstrated how idealized warm Indian Ocean SST anomalies could force southern African rainfall anomalies in an atmosphere-only GCM. Hermes and Reason (2005) further elucidated the air–sea interaction mechanisms by which these anomalies could arise and Ratnam et al. (2015) showed that the peak of these anomalies in JFM was an important factor in southern African summer rainfall. Long-running coupled ocean–atmosphere GCM simulations further confirmed that the SIOD serves to modulate the first-order response to El Niño of drying during the December–March summer rainfall season (Hoell et al. 2017). The conclusion common to these studies is that positive SIOD phases enhance the supply of moisture and negative SIOD phases reduce the supply of moisture to southern Africa in JFM.

Cloud band likelihood may be modified in mid- to late summer by changes in the convective environment in the SICZ, which is linked to these SST anomalies. D'Abreton and Lindesay (1993) demonstrated different circulation anomalies for early (October–December) and late (January–March) summer rainfall anomalies, concluding that the late summer variations were linked to changes to a more tropical rainfall regime, as expected by an increased moisture supply into a convective rainfall regime. Early summer rainfall anomalies showed demonstrable differences in rainfall regime with stronger influence from westerly flow (D'Abreton and Lindesay 1993). We now give attention to this westerly flow.

Regions of enhanced wind speed, jet streams, can act as waveguides to support the development and propagation of synoptic-scale waves. Over southern Africa, waves propagating eastward in the upper-level westerly flow induce lower-tropospheric uplift below the divergent upper-level flow ahead of a trough. This uplift provides the necessary forcing to trigger widespread convection characteristics of TE cloud bands over southern Africa (Harrison 1984; Hart et al. 2010; Macron et al. 2014) and indeed produce the cloud band characteristics of TE interactions elsewhere on Earth (Knippertz 2007). Despite widespread acknowledgment of the importance of such waves, there has been little investigation of the structure of mean westerly flow in which these waves propagate. The main understanding comes from Lindesay (1988) who showed that stronger and northward-shifted westerly flow is characteristic of dry years over subtropical southern Africa. Westerly flow in the subtropics is a result of both tropical forcing and extratropical internal variability, which opens the question as to what forces such a northward shift?

Subtropical jets manifest on the poleward flanks of regions of strong tropical heating and upper-level divergence that deform and sharpen absolute vorticity gradients in the subtropical upper troposphere (Sardeshmukh and Hoskins 1988). In contrast, jets in the extratropical atmosphere support and are, in turn, maintained by baroclinic waves (Hoskins and Valdes 1990). Such eddy-driven jets have a signature of enhanced westerly flow that extends throughout the depth of the troposphere (e.g., Davis and Birner 2013) and, in part, require substantial low-level baroclinicity. The radius and rotation rate of Earth are such that only one to two distinct jet structures can be supported at any given time and often they are a composite of the eddy-driven jet and subtropical jets (Chemke and Kaspi 2015). At the monthly time scales and regional spatial scales considered in this present study, the subtropical jet, the eddy-driven jet, or a composite jet could prevail.

The jet structure of this westerly flow in any given month could have important implications for the frequency, speed, and amplitude of upper-level waves passing over southern Africa. To begin assessment of this possibility, this study will provide a more detailed diagnosis of these jet structures in the South Atlantic–south Indian Ocean sector of the Southern Hemisphere. Marked differences are discovered between El Niño and La Niña seasons, with potential implications for TE cloud band likelihood in the SICZ.

## 3. Data and cloud band identification

### *a. Data*

Daily mean outgoing longwave radiation (OLR) is obtained from the interpolated NOAA Climate Data Record (NCDR-OLR) for the period 1 January 1979–31 December 2012 (Lee 2014). This product interpolates data from the high-resolution infrared radiation sounders flown on the NOAA and MetOp polar-orbiting satellites to a daily 1° × 1° latitude–longitude grid. Geostationary imagers are used to improve the temporal interpolation between swaths (Lee 2014).

An observationally constrained estimate of the circulation and thermodynamics of the atmosphere for the period 1979–2015 is provided by the NCEP–DOE Reanalysis II (NCEP2; Kanamitsu et al. 2002). These data are available on a 2.5° × 2.5° latitude–longitude grid on 17 pressure levels. The results (not shown) using the European Centre for Medium-Range Weather Forecasts interim reanalysis (ERA-Interim; Dee et al. 2011) are qualitatively similar to those reported here.

El Niño and La Niña seasons are defined from the Niño-3.4 index for seasons in which the SST anomaly exceeds ±0.7 of a standard deviation ($\sigma$) from climatology. Similarly SIOD phases are only considered in seasons when the Behera and Yamagata (2001) index exceeds $\pm 0.7\sigma$ concomitant with an ENSO season. The NOAA Optimum Interpolation SST was used to create these indices (Reynolds et al. 2002). El Niño seasons used in this study begin in 1982, 1986, **1987**, *1991*, *1994*, *1997*, 2002, **2006**, and 2009; La Niña seasons begin in 1983, 1984, 1988, 1995, **1998**, *1999*, 2000, 2007, **2010**, and *2011*. Years in bold or italics highlight positive and negative phase SIOD anomalies, respectively.

Statistical significance of the ENSO composite anomalies is determined using Student's $t$ tests at each grid point. False discovery rates (FDR) of significant anomalies are controlled by use of a confidence level based on the distribution of $p$ values from each grid point in the composite map, defined as $p^*_{\mathrm{FDR}}$ (following Ventura et al. 2004; Wilks 2016). The false discovery control level is set at a conservative value, $\alpha_{\mathrm{FDR}} = 0.05$, which yields $p^*_{\mathrm{FDR}} \approx 0.02$ and lower in the composite maps presented. For the cloud band count anomaly composites the FDR step is not applied, as the discontinuous integer field of cloud band count does not yield smooth $p$ value distributions, therefore, a Student's $t$ test is used with $p_{\mathrm{sig}} < 0.02$.

### b. Obtaining a tropical–extratropical cloud band event set

A "metbot" methodology (Hart et al. 2012) is applied to the daily mean OLR data to identify tropical–extratropical cloud bands over southern Africa and the south Indian Ocean. The method identifies contiguous regions of low-valued (deep convective cloud) OLR in a specified domain, which is defined here as 15°–40°S, 7.5°–100°E. The low-value OLR threshold is chosen based on the frequency distribution of OLR values within the domain: the subtropical region produces a bimodal distribution with a frequency peak for clear-sky high pressure regions and a second low-valued peak for deep cloud regions. The OLR threshold is chosen in the saddle between these peaks at $240\,\mathrm{W\,m^{-2}}$ in NCDR-OLR data. Tropical–extratropical cloud bands are then flagged on days in which the contiguous OLR "blobs" (OLR $< 240\,\mathrm{W\,m^{-2}}$) have sufficient latitudinal extent (20°–40°S) and exhibit positive (NW–SE) tilt. Cloud band events are built from the flagged cloud band days: flagged blobs are grouped into single events if they occur on consecutive days within 1000 km.

There are a few modifications to the Hart et al. (2012) methodology. The underlying labeling of contiguous blobs is now performed by the scikit-image Python package (van der Walt et al. 2014), instead of cvblob (Liñán 2008); this change does not affect results. Second, events that produce a large outbreak of deep convection on only a single day are now included in the event set, whereas before this was required as at least two days, even if one of those days was not flagged as a cloud band. This change increases the number of events included. Finally, in order to prevent the spurious single event grouping of a cloud band that develops west (upstream) of a cloud band the previous day, a constraint ensures that events are only created from cloud band blobs that track eastward. There were very few of these spurious events but they are now split into individual events.

### c. Detection of jet axes

The origin of the subtropical jets implies that strong upper-tropospheric westerlies in the subtropics often overlie weak low-level winds. In contrast, the extratropical eddy-driven jet is characterized by baroclinic waves that, in the mean, produce strong westerlies throughout the troposphere (e.g., Davis and Birner 2013). This means that the subtropical jet can be highlighted when the surface zonal wind is subtracted from the full zonal wind at each height (after Davis and Birner 2013). Zonal wind maxima are then identified in both the full zonal wind and the modified zonal wind fields. The latitude and altitude of these maxima are identified with bilinear interpolation to improve accuracy.

Davis and Birner (2013, 2016) applied this procedure to the zonal-mean, time-mean flow in climate models, referring to this baroclinic wind maxima as $U_{\mathrm{max}}$; here it is applied at each longitude in monthly mean data. Identifying the latitude and level of the maxima in the full wind ($U_{\mathrm{full}}$) is used to locate the dominant jet maxima that is typically found in the eddy-driven jet. Only the zonal wind field below the thermal tropopause is considered in order to avoid inclusion of the stratospheric polar vortex. Finally eddy-driven and subtropical jet axes are created by joining (across the individual longitudes) the $U_{\mathrm{full}}$ maxima and $U_{\mathrm{max}}$ maxima, respectively. Zonal continuity of these jet axes is only maintained if the latitude varies by less than 2.5° north or south. Furthermore, whenever a $U_{\mathrm{max}}$ jet axis is within 2.5° of the $U_{\mathrm{mean}}$ jet axis, we consider them as the same jet and only the $U_{\mathrm{mean}}$ axis is shown.

## 4. Tropical–extratropical cloud band likelihood in El Niño and La Niña seasons

In October, 2–3 cloud band days are expected from climatology (black contours, Fig. 1), and there is little modification of this expectation during La Niña. The November La Niña composite shows 1–2 more cloud

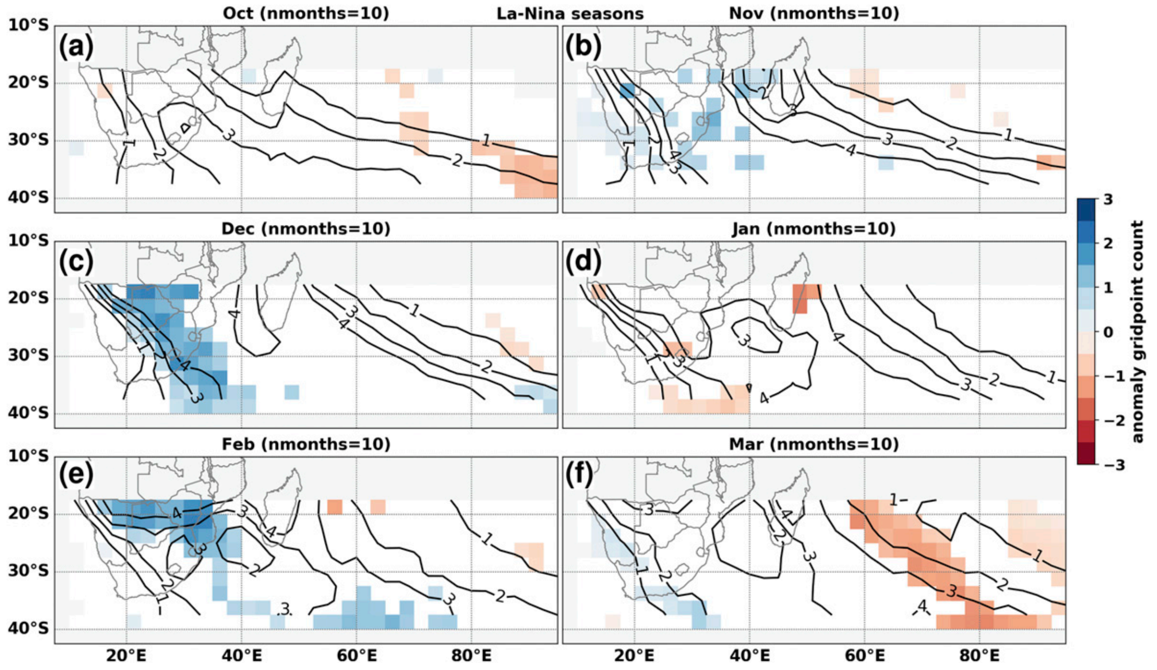

FIG. 1. Cloud band gridpoint count anomalies (shaded) for summer months during the composite La Niña season (computed from 10 seasons). The shading represents the anomaly expressed as the number of times more or less than climatology that cloud bands occur over a particular grid square. The climatology of gridpoint counts per month is contoured (black lines). Shading represents composite anomalies with 98% probability of being distinct from the climatological distribution, as determined by a Student's *t* test.

band days than climatology over southern Africa. This 50% increase in cloud band gridpoint count persists and strengthens into December. In January, the composite signal weakens with negligible modification to climatology, before reemerging in February with twice as many cloud bands expected over southern Africa. During March the composite anomaly shows that no cloud bands are likely in the eastern flank of the SICZ between about 40° and 55°E. In summary, the average expectation for La Niña is for 150%–200% higher cloud band occurrence within the climatological locations for these systems, particularly over mainland southern Africa.

For El Niño composite seasons, cloud bands well east of the climatological regions (as shown by black contours in Fig. 2) are favored with some enhancement over Madagascar in January (Fig. 2). As early as October in the composite El Niño season, cloud bands are found east of climatological expectations. In November, a 25%–50% reduction of cloud band days over the subcontinent becomes evident, persisting weakly into December.

In El Niño Januaries, as with the composite La Niña signal, there is a negligible change to climatology over the southern African mainland. However, over the southwest Indian Ocean there are 1–2 more cloud band days (Fig. 2). During February, an anomaly pattern similar to November manifests, with 50% fewer cloud bands over mainland southern Africa versus a 50% increase in the south Indian Ocean. By March, the signal is confined to enhanced occurrence in the south Indian Ocean, east of the climatological location.

While Figs. 1 and 2 considered the composite response to ENSO seasons, Fig. 3 presents monthly box-and-whisker plots separately for the continental and oceanic cloud band frequencies. Figure 3a shows that during seasons with a neutral ENSO phase cloud band development over mainland southern Africa peaks in November with 3–5 events and this declines to 2–4 events by February. The whiskers in the plot show that while these cloud band counts are most likely, large interannual variations exist.

For cloud band events developing over and east of Madagascar (Fig. 3b) the seasonal cycle is weakly bimodal with peaks in early and late summer at 3–6 events. In general, the interquartile spread in monthly event frequency is broader for the oceanic region than for mainland southern Africa.

During La Niña the seasonal cycle of monthly frequency is maintained and enhanced over southern Africa (Fig. 3c). This is particularly clear in December and February with the observed frequency distributions shifting to an additional 1–2 events per month. Figure 3c demonstrates that the La Niña distributions still overlap the distributions from neutral years. This illustrates that La Niña increases the likelihood of cloud band development,

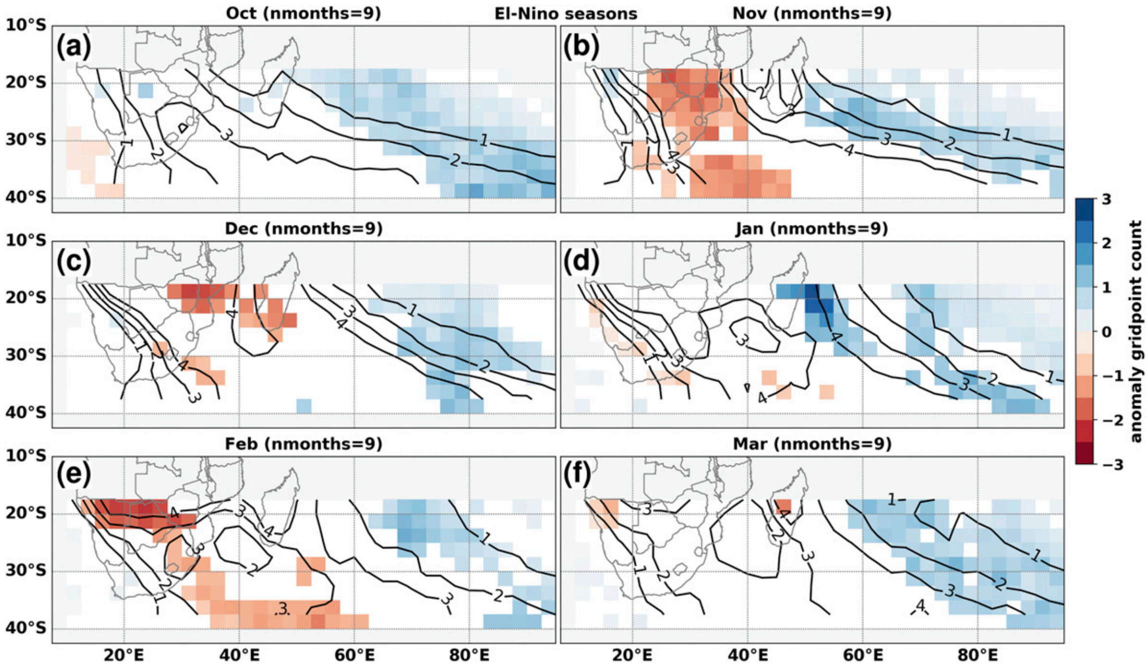

FIG. 2. As in Fig. 1, but for the composite El Niño season (computed from 9 seasons).

but during any given La Niña season climatological numbers of events may well occur. Monthly event frequencies for La Niña Januaries are typically lower than climatology, expressing information that was lost in the composite cloud band gridpoint counts in Fig. 1.

The changes for oceanic cloud band development during La Niña seasons is somewhat different. November has reduced event counts, with an increase in likelihood shown during December to February (Fig. 3d). Again, the widespread in the interquartile range implies a less clear manifestation of a La Niña influence during any individual La Niña season. Nevertheless, the average impact over these 10 La Niña seasons is to modify oceanic cloud band likelihood to a unimodal seasonal cycle with a peak in December. In summary, La Niña seasons are characterized by enhanced cloud band likelihood throughout the SICZ region, however, there is distinct subseasonal variation in when this enhancement is present.

La Niña can be characterized as an enhancement of the global climatological seasonal cycle. In contrast, El Niño presents as a strong spatial perturbation to the seasonal cycle in the Pacific. This change perturbs the Walker Circulation to induce anomalous convection over the central tropical Indian Ocean. This is reflected as a spatial shift in cloud band likelihood in the SICZ with a reduction over the subcontinent and an increase in events over and east of Madagascar (Figs. 3e and 3f). The continental reduction in El Niño seasons is most clear in monthly cloud band frequency for November, December, and February, when 1–2 fewer cloud bands are expected (Fig. 3e). By considering the overlap in distributions it is most likely that November will have fewer events during El Niño seasons than in other seasons. As for La Niña, the El Niño seasons have fewer cloud bands over the subcontinent in January (Fig. 3e).

Figure 3f shows that oceanic cloud bands have marginally lower likelihood of developing in El Niño Novembers as shown by the interquartile range. From December to March, however, there is a shift of the distributions to higher likelihoods of cloud band development, overlapping with the upper ends of the distributions from ENSO-neutral seasons. Comparison with Figs. 2c and 2f shows this is mostly due to events observed east of the climatologically favored location. It is only in January that the enhanced likelihood is concentrated over Madagascar (Fig. 2d).

The phase of significant SIOD anomalies depicted in Fig. 3 shows few systematic associations with departures from cloud band climatology. This suggests SIOD modulation of moisture supply to southern Africa during ENSO seasons can only explain part of the cloud band variability in the region.

It is well established that for tropical–extratropical cloud bands to develop, particularly over subtropical southern Africa, sufficient moisture is needed in the lower troposphere to support convection. This convection organizes along the leading edged of an upper-level wave (Fauchereau et al. 2009; Hart et al. 2010; Macron

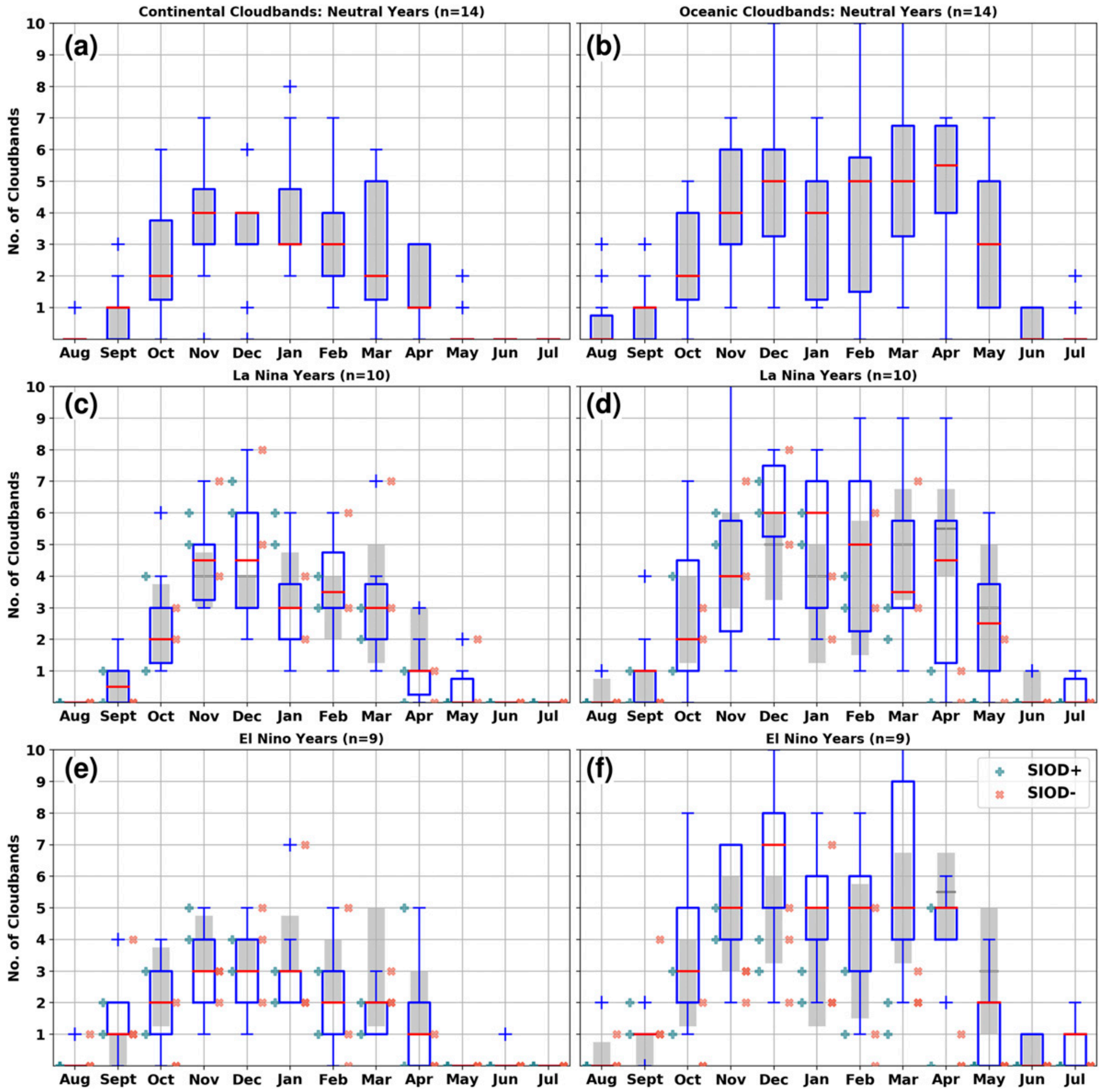

FIG. 3. Seasonal cycle of monthly cloud band count in SICZ split into continental and oceanic events by location, respectively, west or east of 40°E. The distribution of cloud band counts over southern Africa is computed from (a),(b) ENSO-neutral seasons, and plotted for reference (gray boxes) in (c),(d) La Niña seasons and (e),(f) El Niño seasons. The same plots produced for cloud bands in the southwest Indian Ocean are shown in (d) and (f). Red lines denote the median of monthly distribution and the boxes show the interquartile range. Blue "+" and red "×" denote south Indian Ocean dipole (SIOD) positive and negative phases, respectively, plotted for years in which an SIOD event was contemporaneous with either (c),(d) La Niña or (e),(f) El Niño seasons. The *y* coordinate of each the SIOD phase marker shows the respective cloud band count.

et al. 2014). The next two sections address the following question: What changes in convective environments and upper-level flow are associated with the changes in cloud band likelihood during ENSO seasons?

## 5. Convective environments

Differences between the convective environments during positive and negative ENSO events are diagnosed with a measure of the tropospheric instability based on moist static energy $h$: $h = C_p T + L_v q + gz$, where $C_p$ is the specific heat capacity of air, $T$ is temperature, $L_v$ is the latent heat of vaporization, $q$ is specific humidity, $g$ is gravitational acceleration, and $z$ is geopotential height. Moist static energy ($h$) serves as a measure of the internal energy of air parcels and is approximately conserved with parcel motion (Betts 1974). In a stable atmosphere, $h$ will increase with height;

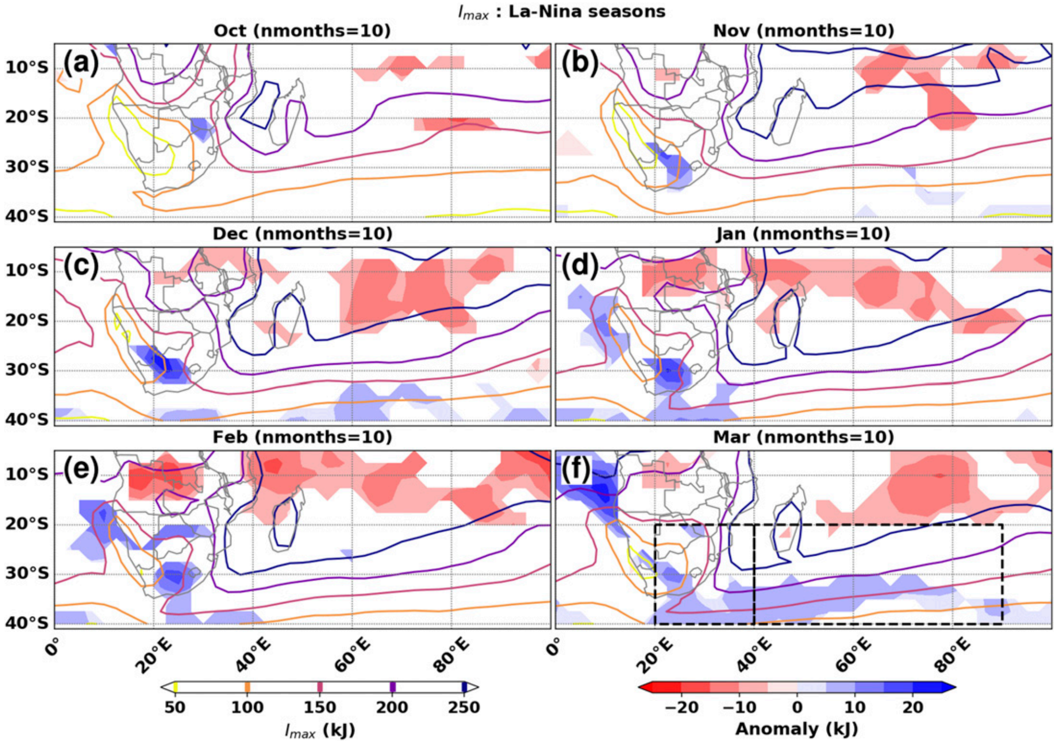

FIG. 4. (a)–(f) Composite anomaly of maximum instability, $I_{\max}$, for La Niña seasons (shaded, kJ). Composite of the full instability field is drawn for reference in colored contours. Boxes used for the mean $I_{\max}$ used in Fig. 6 are drawn in (f). Shaded anomalies are significant as determined by a Student's $t$ test with the false discovery rate controlled by the $p^*_{\mathrm{FDR}}$ value computed with $\alpha_{\mathrm{FDR}} = 0.05$. Composites were computed from 10 La Niña seasons.

however, in a conditionally unstable atmosphere it will decrease, at least within unstable layers. The stratification of moist static energy, $h$, provides a useful diagnosis of the convective environment within the tropics and subtropics. The monthly mean vertical profile of $h$ should be interpreted as both an indication of potential for convection to develop and the average profile produced by convective activity.

We compute maximum tropospheric instability ($I_{\max}$) for each column, as follows:

$$I_{\max} = \int_{\mathrm{sfc}}^{P_{\max}} \frac{dh}{dp}\, dp/g. \qquad (1)$$

First, variables are interpolated onto intermediate levels, which allows evaluation of the vertical derivative $dp$ on the available pressure-level vertical grid of the NCEP2 data. The integral is computed from the surface (sfc) to each layer above the surface up to 100 hPa. The term $P_{\max}$ is the pressure level at which the integral is maximum, giving $I_{\max}$. Since the pressure difference between layers is not always uniform the integral is mass weighted, hence $dp/g$ as the integrating increment. The final result provides a gross measure of maximum instability calculable in a given tropospheric column. This can be considered a simplified version of gross moist stability developed in Yu et al. (1998). To include near-surface instability and appropriately account for topographic variation, the first layer $dh/dp$ is always computed using the reanalysis 2-m $T$ and $q$ and the values on the first pressure level above the surface. The terms contributing to $h$ ($C_pT$, $L_vq$, and $gz$) can be integrated to $P_{\max}$, as defined from Eq. (1), in order to assess the relative contributions to $I_{\max}$. Typically, $P_{\max}$ occurs at ~550 hPa over the mainland southern Africa and ~650 hPa over the Indian Ocean (not shown).

During the composite La Niña season, a region of enhanced instability is established in November in the semiarid western parts of subtropical southern Africa (Fig. 4). This intensifies and expands through to January and February. The signal is located where small east–west shifts in the convective-favorable environment could have large impacts. Consideration of the contributions to instability from temperature and moisture revealed that much of this signal comes from more unstable temperature profiles (not shown). Further north, in the tropics, convection becomes slightly less favored from December to February (Fig. 4e). This is possibly associated with a more southern location of the most

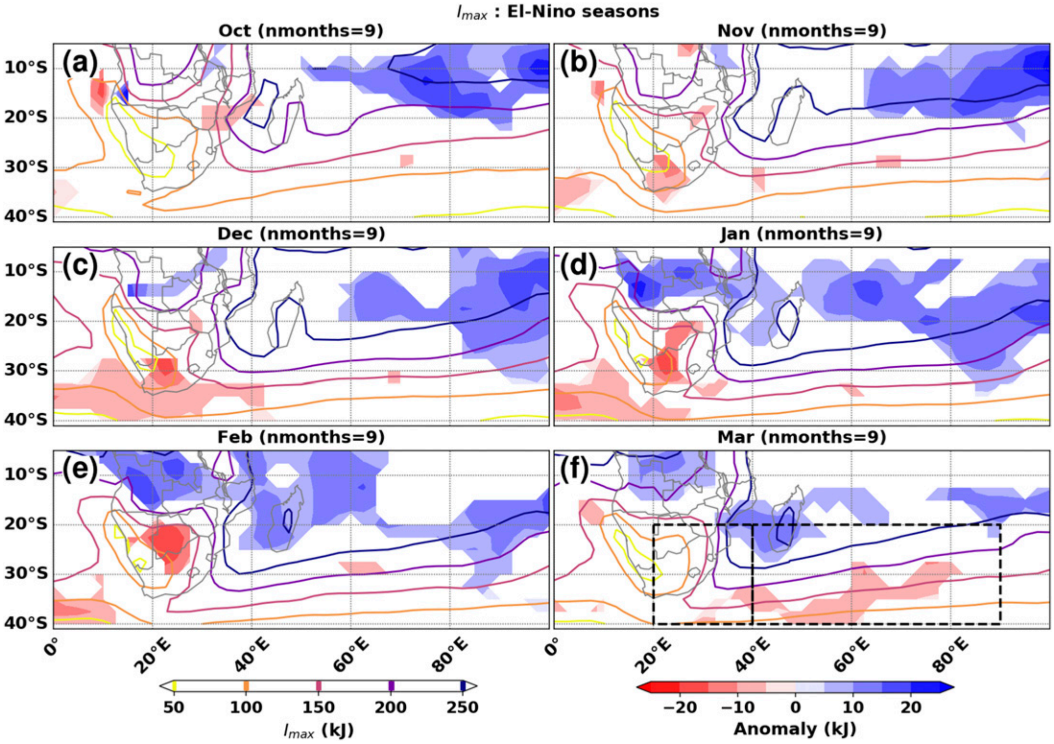

FIG. 5. As in Fig. 4, but for composite El Niño season (computed from 9 seasons).

active convective zone during La Niña seasons. Notably, there is no significant signal in the composite maps through much of the core convective summer rainfall region over mainland southern Africa (~25°–35°E), with a clear signal only seen in the subtropical parts. In the tropical Indian Ocean the atmosphere is anomalously stable during December through March (Fig. 4).

Figure 5 shows the composite for El Niño seasons. The dominant signal, which is already established in October, is of one enhanced instability in the central and eastern tropical south Indian Ocean, indicative of enhanced convection. This zone moves south as the austral summer advances. South of this increased instability a region of reduced instability develops by March in the eastern edge of the SICZ. Over subtropical southern Africa the signal remains weak, but it does suggest a significant reduction of instability over South Africa and parts of Botswana during November through January (Figs. 5b–d). Much of this signal occurs in the semiarid marginal zone where the La Niña composite showed more instability. There is, however, increased instability to the north over tropical southern Africa in January to March, particularly in January and February where the signal extends across to the Tanzanian coast. These instability changes are dominated by increased instability in the temperature profile (not shown), likely diagnosing enhanced convection.

The La Niña and El Niño anomalies in instability are only about 10% above or below the climatological values; however, especially in semiarid areas with marginal convective environments, such changes could shift instability above or below a critical threshold for convection to develop.

To explore the spread in changes to convective environments in the SICZ during ENSO, the area-averaged instability is computed for each month in the continental and oceanic locations of cloud band formation. Figure 6 presents the seasonal cycles of $I_{\max}$ area averaged over the boxes in Fig. 5f, which cover the western and eastern SICZ regions.

Considering neutral ENSO years (Figs. 6a and 6b), the subcontinental domain has an average instability of about 130 kJ in November reaching a maximum about 180 kJ in February before dropping below 120 kJ by May. December exhibits the largest spread in values. Over the oceanic region, a similar seasonal cycle is observed; however, the instability is typically about 20 kJ higher than the subcontinental region. Furthermore, the February peak in $I_{\max}$ over the ocean persists into March and decreases more slowly into May and June. This lag is likely related to the seasonal cycle in sea surface temperature that peaks in March and has a lagged response to seasonal changes in surface heat fluxes.

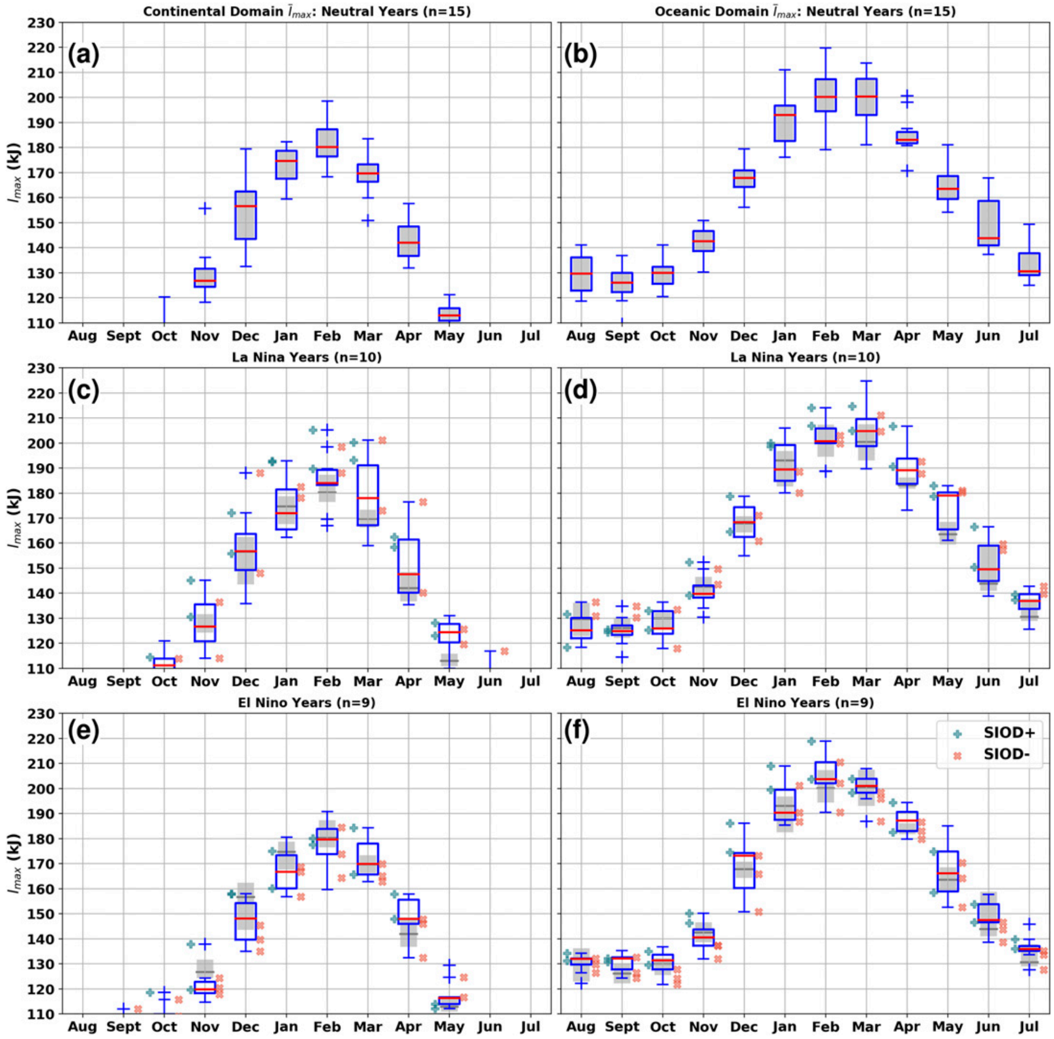

FIG. 6. Seasonal cycle of monthly mean $I_{max}$ split into continental and oceanic regions by location, respectively, west or east of 40°E. Distribution of $I_{max}$ over southern Africa and the south Indian Ocean is computed during (a),(b) ENSO-neutral seasons and is plotted for reference (gray boxes) in (c),(d) La Niña seasons and (e),(f) El Niño seasons. Red lines denote the median of monthly distribution and boxes show the interquartile range. Blue "+" and red "×" denote SIOD positive and negative phases, respectively, plotted for years in which an SIOD event was contemporaneous with an ENSO event. The *y* coordinate of each phase marker shows the respective $I_{max}$ value for each month in the SIOD seasons.

During La Niña, the increased instability observed in the composite (Fig. 4) over southern Africa is borne out in the area-averaged seasonal cycle shown in Fig. 6c. From December to April the La Niña distribution of $I_{max}$ is offset to higher values than those in neutral years.

In contrast, the monthly distributions in the oceanic domain do not show the same clear increased instability. Figure 6d shows, however, a modest increase in the late summer months. Positive SIOD phases are associated with the years that have increased instability (Figs. 6c and 6d).

Figures 6e and 6f show the seasonal cycle in $I_{max}$ distributions observed during El Niño events. Over the subcontinent, the instability distribution for El Niño Novembers is almost entirely below the neutral-season distribution with ~10% less instability (Fig. 6e). This reduction persists into January, however, there is substantial overlap with the distribution of neutral seasons. The whiskers for February indicate there have been El Niño seasons with lower instability, but the weight of the distribution remains close to values observed in neutral seasons. When considering the oceanic domain the modification of the seasonal cycle is even less coherent, with much overlap between neutral season and El Niño season distributions (Fig. 6f). Nevertheless, the increase in instability over the ocean in February is

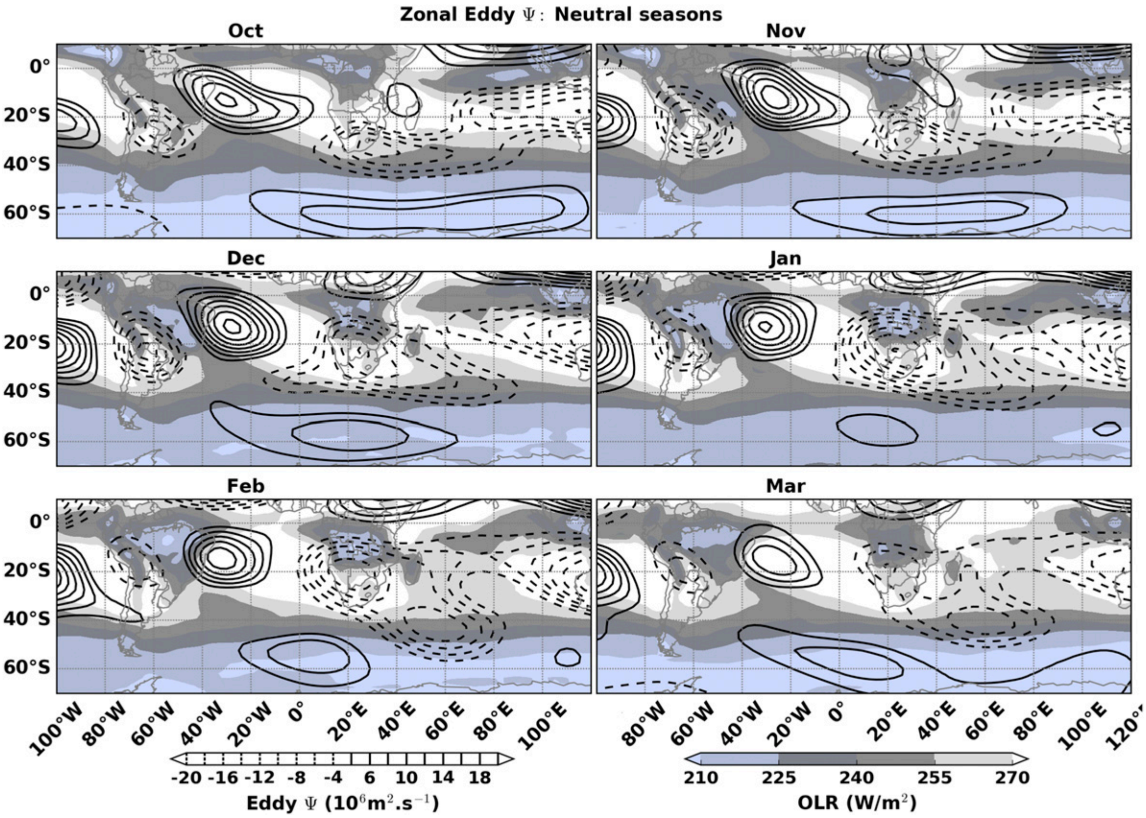

FIG. 7. Monthly mean outgoing longwave radiation (shaded, W m$^{-2}$) and zonal eddy streamfunction at 200 hPa (contoured with negative values dashed, every $2 \times 10^6$ m$^2$ s$^{-1}$) for the composite ENSO-neutral season.

pronounced, a signal missing from the composite map (Fig. 5e). Figures 6e and 6f demonstrate that strong negative SIOD events further reduce convective instability over mainland southern Africa during El Niño events, corroborating other studies (e.g., Hoell et al. 2017). As expected, positive SIOD events seem to mitigate reductions in the atmospheric instability (Figs. 6e and 6f).

What is clear from Figs. 4–6 is that the strongest anomalies in the subtropics are related to shifts in regions with sharp gradients, and there are only small changes in convective instability in the core SICZ rainfall regions.

This seasonal cycle in instability with the peak occurring in January and February has been shown using radiosonde data (Dyson et al. 2015) and convective available potential energy computed in reanalysis data (Blamey et al. 2017). Both the study of Dyson et al. (2015) and Blamey et al. (2017) demonstrate, however, that environments favorable for severe convection tend to be earlier in summer. They concluded that this seasonality is due to the higher vertical wind shear associated with the presence of upper-level jets. Upper-level flow and regional jet axes are diagnosed in the following section.

## 6. Upper-level circulation and regional jet axes

Since TE cloud bands require upper-level waves in the subtropics, it is worth considering whether the jet structures that serve as waveguides for these waves are of subtropical or eddy-driven origin. Next, we diagnose whether local forcing of a regional subtropical jet is plausible and how this might change during ENSO seasons.

The upper-level flow response to tropical heating is well captured in the zonal eddy streamfunction ($\Psi^*$) at the 200-hPa pressure level. Since the zonal mean streamfunction ($\Psi$) is removed, this field highlights the zonal asymmetry in the circulation. Figure 7 presents the mean seasonal progression of 200-hPa $\Psi^*$ and OLR through austral summer, composited from ENSO-neutral seasons. In October, a broad region of negative $\Psi^*$ highlights the anticyclonic shear in the upper-level flow over southern Africa and the southwest Indian Ocean. Monthly mean OLR highlights the movement of

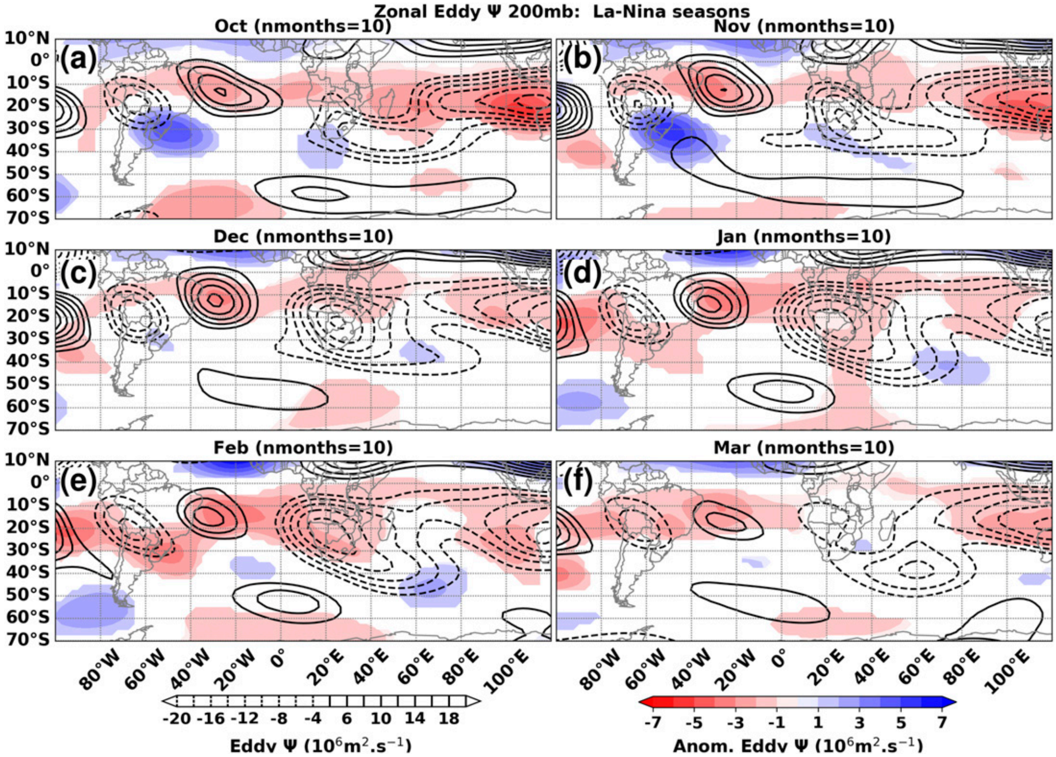

FIG. 8. Full zonal eddy streamfunction at 200 hPa (contoured with negative values dashed, every $2 \times 10^6$ m$^2$ s$^{-1}$) and anomalies (shaded). Shaded anomalies are significant as determined by a Student's $t$ test with the false discovery rate controlled by the $p^*_{\mathrm{FDR}}$ value computed with $\alpha_{\mathrm{FDR}} = 0.05$. Composites are computed from 10 La Niña seasons.

tropical convection into southern Africa through November and December. An upper-level anticyclone centered on subtropical southern Africa develops concomitant with this southward shift and concentration of regional tropical convection in the Congo basin.

Similarly, over South America an upper-level anticyclone, the Bolivian high (Lenters and Cook 1997), gains definition as summertime convection intensifies over Amazonia as implied by the decrease in OLR values from October to January (Fig. 7). The southwest–northeast tilt of the upper-level Gill-type response to tropical heating over South America, creates a situation with strong upper-level cyclonic circulation, the Nordeste low, over the western tropical Atlantic (Lenters and Cook 1997).

Over Africa the response is more symmetric about the equator with an anticyclone over North Africa (Fig. 7, positive values of Ψ indicate anticyclones in Northern Hemisphere), corresponding well to the simplified theoretical solutions of Gill (1980). As tropical convection weakens and starts migrating northward during February and March, the upper-level anticyclones also weaken (Fig. 7).

The large-scale composite response in La Niña seasons shows enhanced convective activity in the tropical heating hotspots. The concomitant enhancement of anticyclonic upper-level circulation is demonstrated through all months in the tropics (Fig. 8, red shading).

The anomalies in upper-level flow during La Niña is most obvious in the eastern Indian Ocean: increased convective heating over the Maritime Continent amplifies the upper-level anticyclone here (Fig. 8). Strong changes are also seen over South America with a strong dipole in $\Psi^*$ anomalies highlighting the weakening of the Nordeste low, and more cyclonic circulation to the southeast of the Bolivian high. Similarly, during El Niño seasons (Fig. 9), the largest $\Psi^*$ anomalies are a weakening of the anticyclone near the Maritime Continent, and a displacement and modulation of the Bolivian high–Nordeste low structure over South America. This seasonal evolution of the ENSO response over South America was shown in 200-hPa Ψ anomalies by Grimm (2003), and is closely tied to primary modes of South American rainfall variability (Grimm and Zilli 2009).

During La Niña seasons over southern Africa, the magnitude of the tropical anticyclonic $\Psi^*$ anomaly is

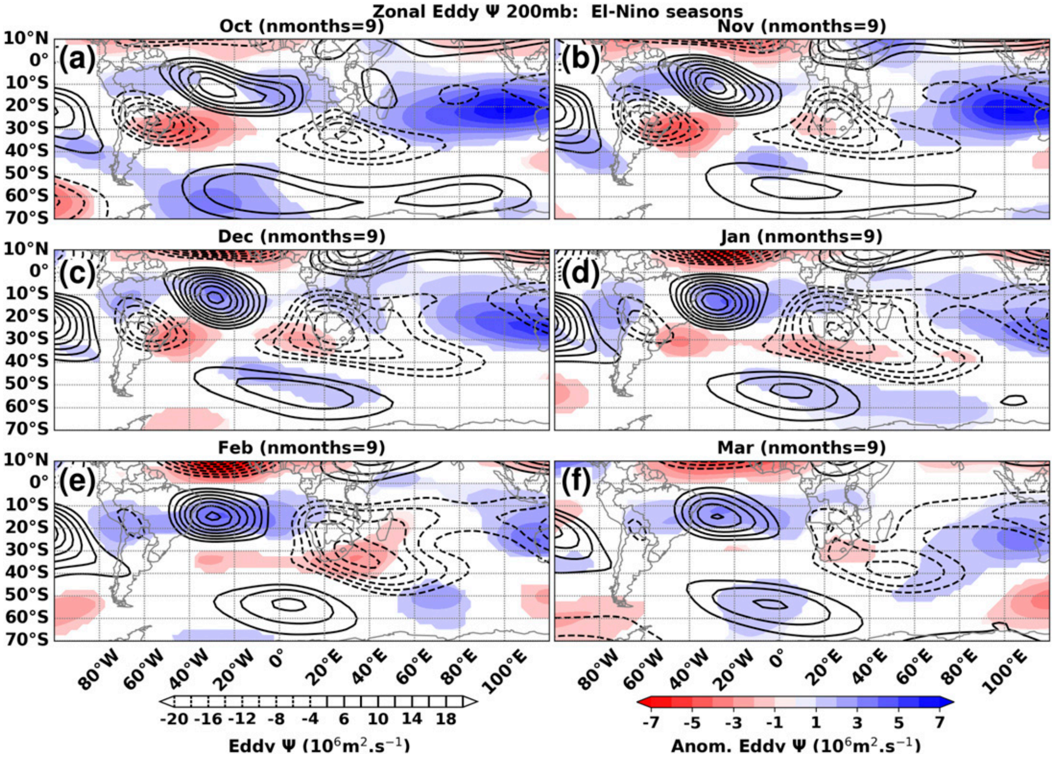

FIG. 9. As in Fig. 8, but for composite El Niño season (computed from 9 seasons).

weaker than the Maritime Continent or South American anomalies. Nevertheless, there is enhancement of the climatological development of the upper-level anticyclone over southern Africa (dashed contours in Fig. 8) during December and January. Along the poleward edge of the 200-hPa anticyclone, positive anomalies indicate reduction in anticyclonic shear here in early summer (Figs. 8a and 8b). In the El Niño composite (Fig. 9), cyclonic flow anomalies weaken the tropical upper-level anticyclone over southern Africa, especially in December and January. The anticyclonic shear in the flow south of Africa is increased throughout summer months. Thus, changes in $\Psi^*$ over southern Africa are broadly opposite between ENSO phases.

Reason (2016) and Driver and Reason (2017) showed a strong weakening during La Niña and strengthening during El Niño of the midlevel Botswana high, something not seen here in the 200-hPa $\Psi^*$ anomalies. However, this midlevel response is obvious in $\Psi^*$ anomalies at 500 hPa (not shown). The contrast highlights that the subtropical troposphere is not equivalently barotropic through its full depth: 200-hPa circulation highlights divergent tropical outflow and the descent of this outflow is well captured at 500 hPa in the subtropics (e.g., Schwendike et al. 2014). Results presented here are focusing on the upper-level outflow.

The stronger local upper-level anticyclones associated with stronger divergent outflow during La Niña seasons may enhance subtropical upper-level westerlies locally, following the arguments of Sardeshmukh and Hoskins (1988). Similarly, the weakened tropical anticyclone during El Niño seasons may present weaker tropical forcing of subtropical upper-level gradients, leading to weaker upper-level flow over subtropical southern Africa.

The strong ENSO anomalies in upper-level flow over South America could also modify the downstream flow associated with cloud bands over southern Africa as suggested by Harrison (1986) and Tyson (1986). These authors proposed that angular momentum exported from tropical South America by tropical–extratropical interactions would lead to equatorward recurvature of the mean flow by conservation of momentum. Where this recurvature occurred would be set by the magnitude of momentum export and could suppress or enhance southern African rainfall. Idealized GCM simulations supported this view (Cook et al. 2004). Grimm and Reason (2011, 2015) demonstrated interannual and intraseasonal connections, respectively, between South American and South African rainfall and more recently Puaud et al. (2017) showed covariability of cloud band development over each continent.

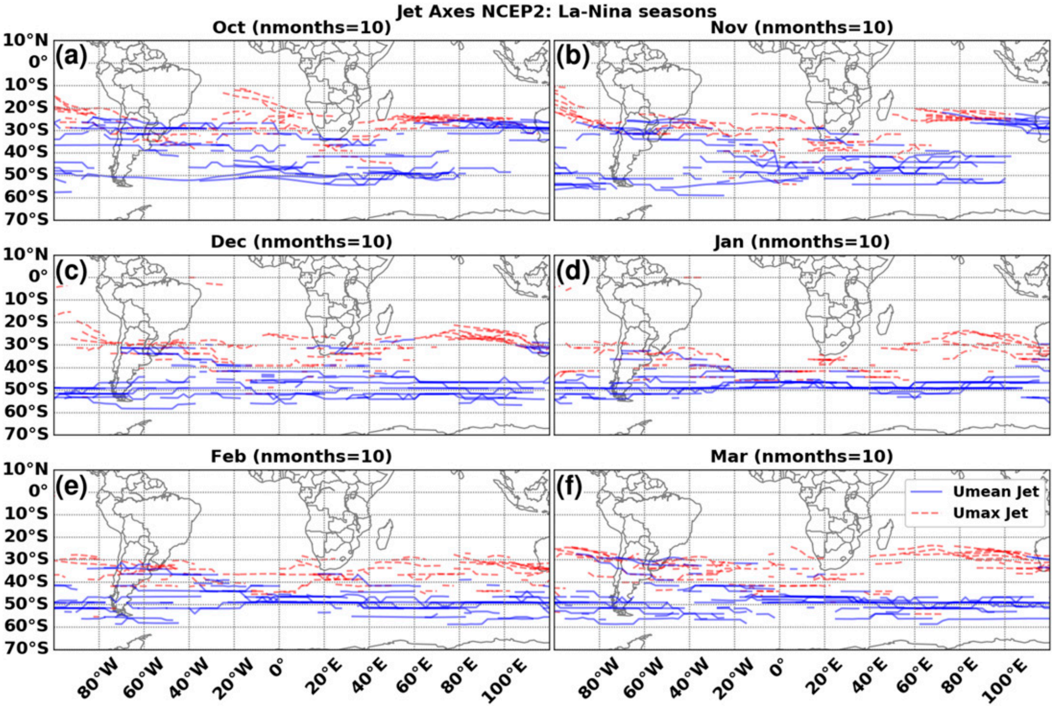

FIG. 10. All eddy-driven jet axes (solid blue) and distinguishable (see text) subtropical jet axes (red dashed) from 10 La Niña seasons.

To see whether there are indeed changes in the eddy-driven and subtropical jets forced locally or remotely, Figs. 10 and 11 present the jet axes during La Niña and El Niño seasons, respectively. Axes from all the respective seasons are included and as such, the maps provide the full range of ENSO responses in jet axis presence and location during a given month.

The jet axes over South America are characterized by jet locations likely in the subtropics near 30°S and across the high-latitude Southern Ocean (Fig. 10). However, during El Niño months, the likelihood of high-latitude eddy-driven jet axes is diminished, particularly during November and December (Fig. 11).

For La Niña seasons, subtropical jets are common across the South Atlantic and south Indian Oceans with indication of an eddy-driven jet south of southern Africa (Fig. 10). North of these eddy-driven jet axes, distinct subtropical jets over southern Africa are common in November and December and again in February. During January, subtropical jets are present just south of the subcontinent. The contrast to El Niño seasons (Fig. 11) is striking: there is some likelihood of southern African subtropical jets during November but they are indistinct from the eddy-driven jet. This persists until March. This may be linked to the generally reduced strength of the divergent outflow and 200-hPa anticyclone during El Niño years, as noted in the discussion of $\Psi^*$ anomalies, or perhaps related to the upstream changes over South America.

With more focus on the jet configurations local to southern Africa, Fig. 12 considers the separation between barotropic ($U_{\mathrm{mean}}$) and baroclinic ($U_{\mathrm{max}}$) zonal wind maxima computed from the zonal mean of zonal wind over southern Africa (15°–35°E). The seasonal cycle of this separation during seasons that develop during La Niña and El Niño conditions is presented in Figs. 12a and 12b, respectively. This figure quantifies the visual separation between jet axes in Figs. 10 and 11 in the southern African sector.

Differences between ENSO phases already exist in spring, where La Niña seasons demonstrate a wide spread between $U_{\mathrm{mean}}$ and $U_{\mathrm{max}}$ latitudes, with separations of 5°–10° latitude likely (Fig. 12a). Larger separations are likely in October and November, with January to March having lower separations. By April, a large separation is reestablished as the eddy-driven jet becomes well established at higher latitudes.

In contrast during El Niño seasons, the $U_{\mathrm{mean}}$–$U_{\mathrm{max}}$ latitudinal separation remains below 5° in November and December (Fig. 12b). In February and March the distributions of possible separations broaden with wider interquartile ranges estimated.

There is no clear indication that the phase of the SIOD has much influence on jet separation (Fig. 12).

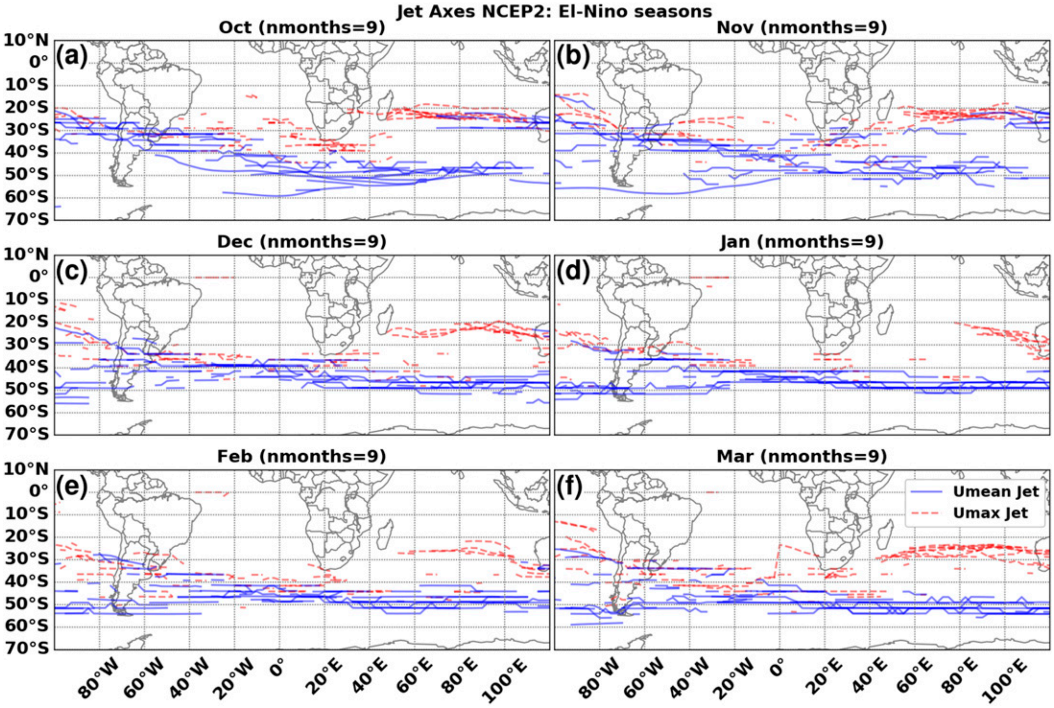

FIG. 11. As in Fig. 10, but for 9 El Niño seasons.

This implies some independence between the influence of Indian Ocean SSTs anomalies on southern Africa and influence from changes in the structure of upper-level westerly flow over the region.

It is apparent from Fig. 12, that La Niña and El Niño show distinct seasonal evolutions with differences in the strength of circulation perturbations during early versus late summer, as was also suggested by the results in Figs. 10–11. The differences in the jet axes imply differences in waveguides between positive and negative ENSO phases. The next section examines whether these monthly mean differences manifest in the synoptic-scale convective activity associated with tropical–extratropical cloud band development, particularly over mainland southern Africa.

## 7. Synoptic-scale changes in tropical–extratropical cloud band events during ENSO seasons

Section 5 diagnosed particularly strong enhancement of the convective environment over the semiarid parts of western South Africa, southern Namibia, and Botswana during La Niña seasons. Section 6 showed the presence of a distinct subtropical jet during La Niña seasons but not during El Niño. Do these mean-state changes manifest in the synoptic-scale characteristics of TE cloud bands?

Figure 13 presents the normalized probability distributions of the mean OLR of each ENSO-season TE cloud band that formed over mainland southern Africa (west of 40°E). Separate distributions were calculated for La Niña and El Niño cloud band events, shown in blue and red, respectively. Continental cloud bands that develop more frequently (50 events) during La Niña Decembers typically have warmer cloud-top temperatures, suggesting less deep convection than the fewer (30 events) that formed during El Niño seasons. This may be due to more frequent events forming across the subcontinent in more marginal convective environments (see Figs. 1c and 4c) in which convection, while occurring, covers less area and may not develop very cold cloud top temperatures. Together, these characteristics would result in higher mean daily OLR and since there are more events than in El Niño seasons this could explain the OLR distribution differences.

However, by February more widespread instability is present as a result of both the seasonal increase and addition of La Niña anomalies (Fig. 4e). This enhancement of convective environments—reduction during El Niño—is borne out in Fig. 13e: distinctly lower mean OLR is typically of February cloud bands during La Niña seasons. The OLR minima within cloud bands is also lower in La Niña Februaries (not shown) indicating the increased likelihood of more intense deep convective structures

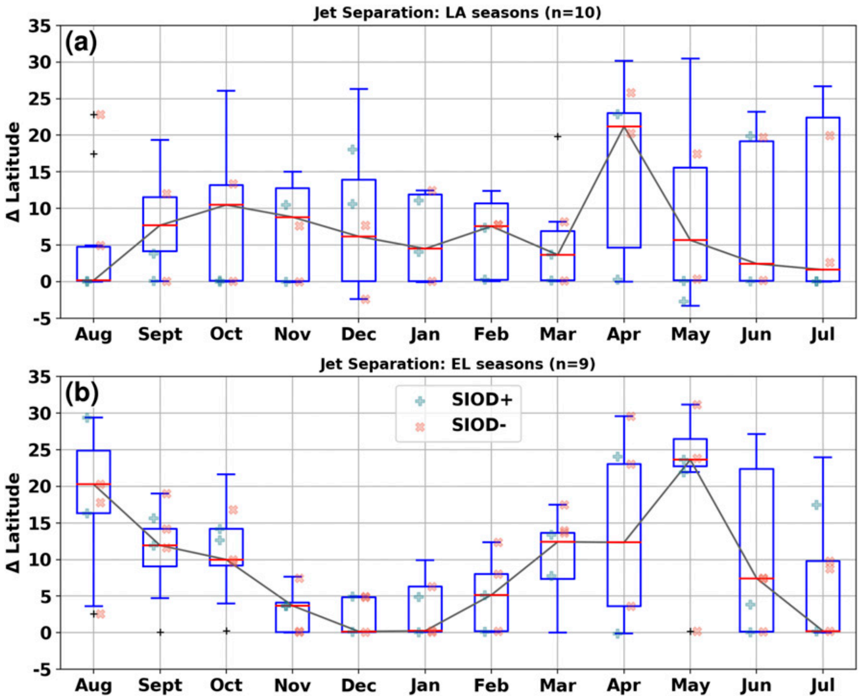

FIG. 12. The latitudinal separation between the eddy-driven jet and the subtropical jet considered in the zonal mean of westerly flow over southern Africa (15°–35°E) during (a) La Niña seasons and (b) El Niño seasons. Interquartile range is shown by boxes with the median indicated in red. Blue "+" and red "×" denote SIOD positive and negative phases, respectively, plotted for years in which an SIOD event was contemporaneous with an ENSO event. The *y* coordinate of each phase marker shows the respective jet separation for each month in the SIOD seasons.

embedded within tropical–extratropical cloud bands when compared to El Niño Februaries. Note that Fig. 13 only considers changes in the convection within continental cloud bands; the only distinct change for oceanic cloud bands is lower mean OLR in events forming during La Niña Januaries (not shown).

These results show that the mean-state perturbations associated with ENSO-season cloud band likelihood are also expressed in meteorological characteristics of the TE cloud bands that form in these perturbed environments.

## 8. Summary

This study set out to understand the impact ENSO events have on TE cloud band likelihood in the SICZ. An object-based cloud band identification methodology enabled the first month-by-month analysis of cloud band occurrence during ENSO-neutral, La Niña, and El Niño seasons. La Niña events are associated with 2–3 more cloud bands per month over mainland southern Africa and the southwest Indian Ocean, particularly in December and February. El Niño events tend to have reduced cloud band likelihood over southern Africa, particularly in November and February, with 1–2 fewer events. In contrast, likelihood in the southwest Indian Ocean is increased by 3–4 events during El Niño. Both positive and negative ENSO events show reduction in cloud band likelihood during January; however, the signal is not significantly outside the range of internal variability in cloud band count.

Two diagnostics of the mean-state, mean convective environments and upper-level subtropical jet streams, are shown to play a role in this variability in cloud band likelihood. A synthesis of these findings are presented in the schematic of Fig. 14, which focuses specifically on continental cloud bands.

The mean seasonal cycle of TE cloud bands (thick gray curve) peaks in November before slowly decaying through summer (Fig. 14). This cycle is not necessarily observed in any given season; it is the climatological likelihood. Substantial interannual variability in monthly cloud band counts is demonstrated by the wide band of gray shading, with two individual example seasons shown in the dashed lines.

The seasonal cycle of the pertinent circulation diagnostics are shown in the bottom panel of Fig. 14.

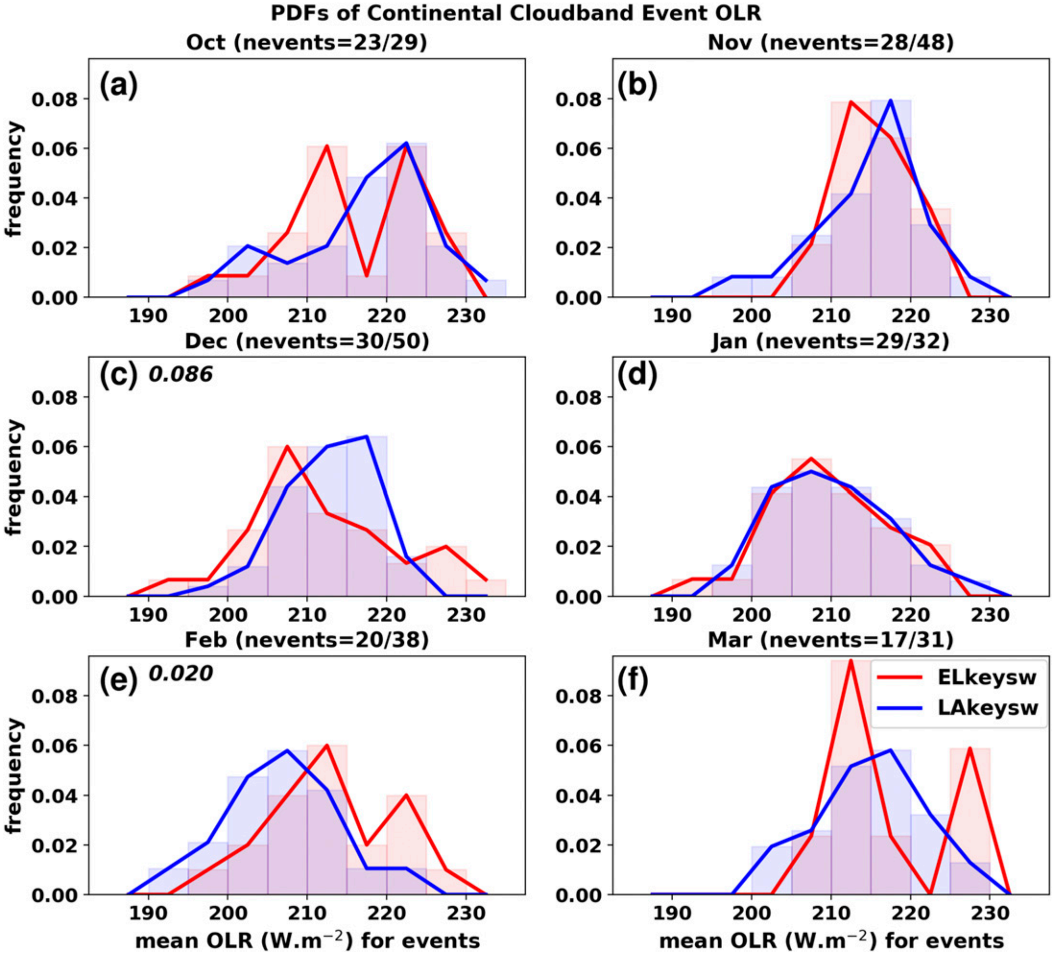

FIG. 13. The distribution of the mean OLR within the blob of each continental cloud band event. Distributions are created from all continental (western) events in a given month during La Niña (blue) and El Niño (red) seasons. The $p$ value from a Kolmogorov–Smirnov test is shown when the La Niña and El Niño distributions have at least an 85% chance of being distinct.

Instability favoring convection (orange curve) increases from October to reach a peak in February. In contrast, subtropical jets (blue curve) are most likely over the continent in spring, least likely in midsummer, before becoming likely again in April. The superposition of the seasonal cycle in these two diagnostics provides an explanation for the November peak in cloud bands and subsequent decay. Early in the season, waves in the upper-level flow start to trigger widespread TE cloud band convection as soon as sufficient lower-tropospheric instability develops. As the atmosphere grows more unstable into midsummer the reduced likelihood of jets and associated changes in upper-level waves means fewer large-scale TE cloud bands are likely to form. While not studied here, the increased convective instability likely supports more local convection, which can be triggered by the diurnal cycle, especially over elevated terrain, and by local low-level convergence.

Despite the modest sample size of ENSO events, the clearest El Niño signal that emerged is of drastic reduction in the likelihood of a regional subtropical jet during summer months (Fig. 11). This is illustrated in Fig. 14 (blue dashed curve) and contrasts with both the climatological expectation of subtropical jets and the likelihood during La Niña (blue dotted curve). Additionally, small reductions in convective instability early in El Niño seasons could drop instability below critical thresholds for development of cloud band–linked convection in the more arid parts of subtropical southern Africa (orange dashed curve). Negative SIOD phases reinforced this reduction of instability during El Niño seasons. Convective environments during La Niña were strongly enhanced over southern Africa especially in the semiarid central southwest (orange dotted curve). SIOD positive phases were associated with a further increase in mean convective

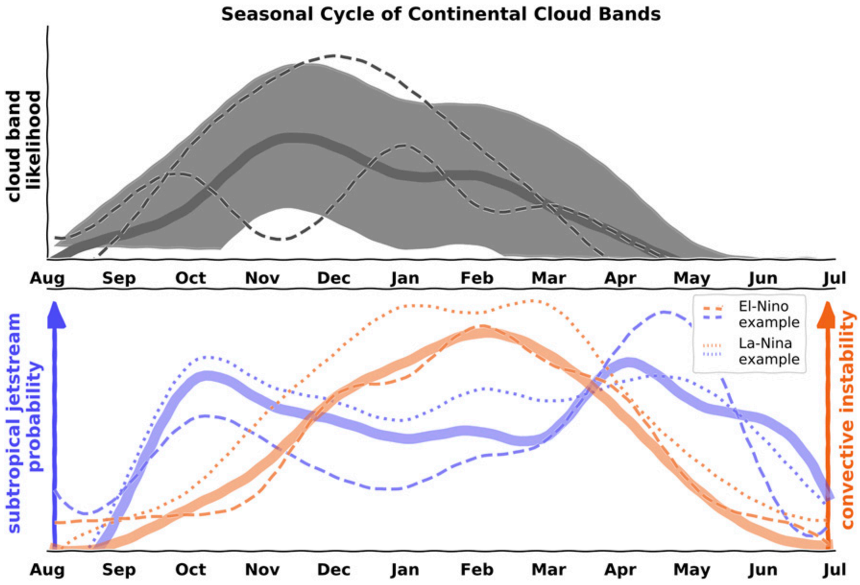

FIG. 14. (top) The mean seasonal cycle in cloud band likelihood is shown schematically (thick gray line). The spread in possible cloud band occurrence is shown (broad gray region) and further reinforced by examples of individual seasons (gray dashed). (bottom) The seasonal cycle in the likely presence of subtropical jet streams (thick blue curve) and convective instability (thick orange curve), which favor the development of TE cloud bands, particularly in early summer. Example perturbations to the seasonal cycle in cloud band–favoring conditions are illustrated for an El Niño (dashed) and La Niña season (dotted).

instability. Further analysis has showed that these mean-state changes were also evident in the synoptic-scale diagnostics of cloud bands. La Niña seasons helped support early season cloud bands in more marginal convective zones and enhanced the intensity of late summer cloud bands, when compared to cloud bands in El Niño seasons.

Our analysis of the seasonal cycle suggests that an ENSO influence on the SICZ may be dominated by westerly jet structure changes in early summer. In mid to late summer, the local SST anomalies and changes in the south Indian Ocean high will modify the convective environments in the SICZ. Grimm (2003) reached a similar conclusion for the remote versus local forcing of South American rainfall. Furthermore, this late summer influence, will more likely manifest in locally forced convection as well and not only in the large-scale TE cloud bands.

This framing of the seasonal cycle provides a novel synthesis of the established understanding for the region. The results presented in this study have reinforced a paradigm that TE cloud bands over southern Africa are a result of a complex interaction between tropical and extratropical processes in the unique environment that establishes in the subtropics.

The seasonality of TE cloud band likelihood emerges from the finely tuned interaction between the asynchronous seasonal cycles in subtropical upper-level westerlies and lower-tropospheric instability. ENSO events likely disturb these seasonal cycles through direct modification of the atmospheric flow and indirectly through modification of local SST anomalies. These conclusions represent important advances to further our understanding of the mechanisms by which tropical Pacific SST anomalies are communicated to southern Africa. Furthermore, this study has pointed to the need for detailed analysis of the seasonal cycles produced by climate models in order to understand and address deficiencies in the simulation of southern African climate.

*Acknowledgments.* Interpolated OLR data, NOAA Optimally Interpolated SST v2, and NCEP Reanalysis-2 data were provided by the NOAA/OAR/ESRL PSD, Boulder, Colorado, from their website (http://www.esrl.noaa.gov/psd/). Two anonymous reviewers are warmly thanked for their thorough reviews and constructive comments that have strengthened this manuscript. This work was carried out under the Future Climate for Africa UMFULA project, with financial support from the U.K. Natural Environment Research Council (NERC), NE/M020207/1 (NCGH and RW) and NE/M020223/1 (CJCR), and the U.K. Government's Department for International Development (DfID).

## REFERENCES

Behera, S. K., and T. Yamagata, 2001: Subtropical SST dipole events in the southern Indian Ocean. *Geophys. Res. Lett.*, **28**, 327–330, https://doi.org/10.1029/2000GL011451.

Betts, A. K., 1974: Further comments on "A comparison of the equivalent potential temperature and the static energy." *J. Atmos. Sci.*, **31**, 1713–1715, https://doi.org/10.1175/1520-0469(1974)031<1713:FCOCOT>2.0.CO;2.

Blamey, R. C., C. Middleton, C. Lennard, and C. J. C. Reason, 2017: A climatology of potential severe convective environments across South Africa. *Climate Dyn.*, **49**, 2161–2178, https://doi.org/10.1007/s00382-016-3434-7.

Chemke, R., and Y. Kaspi, 2015: The latitudinal dependence of atmospheric jet scales and macroturbulent energy cascades. *J. Atmos. Sci.*, **72**, 3891–3907, https://doi.org/10.1175/JAS-D-15-0007.1.

Colberg, F., C. J. C. Reason, and K. Rodgers, 2004: South Atlantic response to El Niño–Southern Oscillation induced climate variability in an ocean general circulation model. *J. Geophys. Res.*, **109**, C12015, https://doi.org/10.1029/2004JC002301.

Cook, K. H., 2000: The South Indian convergence zone and interannual rainfall variability over southern Africa. *J. Climate*, **13**, 3789–3804, https://doi.org/10.1175/1520-0442(2000)013<3789:TSICZA>2.0.CO;2.

——, 2001: A Southern Hemisphere wave response to ENSO with implications for southern Africa precipitation. *J. Atmos. Sci.*, **58**, 2146–2162, https://doi.org/10.1175/1520-0469(2001)058<2146:ASHWRT>2.0.CO;2.

——, J.-S. Hsieh, and S. M. Hagos, 2004: The Africa–South America intercontinental teleconnection. *J. Climate*, **17**, 2851–2865, https://doi.org/10.1175/1520-0442(2004)017<2851:TAAIT>2.0.CO;2.

D'Abreton, P., and J. Lindesay, 1993: Water vapour transport over southern Africa during wet and dry early and late summer months. *Int. J. Climatol.*, **13**, 151–170, https://doi.org/10.1002/joc.3370130203.

Davis, N. A., and T. Birner, 2013: Seasonal to multidecadal variability of the width of the tropical belt. *J. Geophys. Res. Atmos.*, **118**, 7773–7787, https://doi.org/10.1002/jgrd.50610.

——, and ——, 2016: Climate model biases in the width of the tropical belt. *J. Climate*, **29**, 1935–1954, https://doi.org/10.1175/JCLI-D-15-0336.1.

Dee, D. P., and Coauthors, 2011: The ERA-Interim reanalysis: Configuration and performance of the data assimilation system. *Quart. J. Roy. Meteor. Soc.*, **137**, 553–597, https://doi.org/10.1002/qj.828.

Driver, P., and C. J. C. Reason, 2017: Variability in the Botswana High and its relationships with rainfall and temperature characteristics over southern Africa. *Int. J. Climatol.*, **37**, 570–581, https://doi.org/10.1002/joc.5022.

Dyson, L. L., J. Van Heerden, and P. D. Sumner, 2015: A baseline climatology and sounding-derived parameters associated with heavy rainfall over Gauteng, South Africa. *Int. J. Climatol.*, **35**, 114–117, https://doi.org/10.1002/joc.3967.

Fauchereau, N., B. Pohl, C. Reason, M. Rouault, and Y. Richard, 2009: Recurrent daily OLR patterns in the Southern Africa/Southwest Indian Ocean region, implications for South African rainfall and teleconnections. *Climate Dyn.*, **32**, 575–591, https://doi.org/10.1007/s00382-008-0426-2.

Gill, A. E., 1980: Some simple solutions for heat-induced tropical circulation. *Quart. J. Roy. Meteor. Soc.*, **106**, 447–462, https://doi.org/10.1002/qj.49710644905.

Griffiths, G. M., M. J. Salinger, and I. Leleu, 2003: Trends in extreme daily rainfall across the South Pacific and relationship to the South Pacific Convergence Zone. *Int. J. Climatol.*, **23**, 847–869, https://doi.org/10.1002/joc.923.

Grimm, A. M., 2003: The El Niño impact on the summer monsoon in Brazil: Regional processes versus remote influences. *J. Climate*, **16**, 263–280, https://doi.org/10.1175/1520-0442(2003)016<0263:TENIOT>2.0.CO;2.

——, and M. T. Zilli, 2009: Interannual variability and seasonal evolution of summer monsoon rainfall in South America. *J. Climate*, **22**, 2257–2275, https://doi.org/10.1175/2008JCLI2345.1.

——, and C. J. C. Reason, 2011: Does the South American monsoon influence African rainfall? *J. Climate*, **24**, 1226–1238, https://doi.org/10.1175/2010JCLI3722.1.

——, and ——, 2015: Intraseasonal teleconnections between South America and South Africa. *J. Climate*, **28**, 9489–9497, https://doi.org/10.1175/JCLI-D-15-0116.1.

Harangozo, S. A., and M. S. J. Harrison, 1983: On the use of synoptic data in indicating the presence of cloud bands over southern Africa. *S. Afr. J. Sci.*, **79** (10), 413–414.

Harrison, M. S. J., 1984: A generalized classification of South African rain-bearing synoptic systems. *J. Climatol.*, **4**, 547–560, https://doi.org/10.1002/joc.3370040510.

——, 1986: A synoptic climatology of South African rainfall variations. Ph.D. thesis, University of Witwatersrand, 341 pp.

Hart, N. C. G., C. J. C. Reason, and N. Fauchereau, 2010: Tropical–extratropical interactions over southern Africa: Three cases of heavy summer season rainfall. *Mon. Wea. Rev.*, **138**, 2608–2623, https://doi.org/10.1175/2010MWR3070.1.

——, ——, and ——, 2012: Building a tropical–extratropical cloud band metbot. *Mon. Wea. Rev.*, **140**, 4005–4016, https://doi.org/10.1175/MWR-D-12-00127.1.

——, ——, and ——, 2013: Cloud bands over southern Africa: Seasonality, contribution to rainfall variability and modulation by the MJO. *Climate Dyn.*, **41**, 1199–1212, https://doi.org/10.1007/s00382-012-1589-4.

Hermes, J. C., and C. J. C. Reason, 2005: Ocean model diagnosis of interannual coevolving SST variability in the south Indian and South Atlantic Oceans. *J. Climate*, **18**, 2864–2882, https://doi.org/10.1175/JCLI3422.1.

——, and ——, 2009: Variability in sea-surface temperature and winds in the tropical south-east Atlantic Ocean and regional rainfall relationships. *Int. J. Climatol.*, **29**, 11–21, https://doi.org/10.1002/joc.1711.

Hoell, A., C. Funk, T. Magadzire, J. Zinke, and G. Husak, 2015: El Niño–Southern Oscillation diversity and southern Africa teleconnections during austral summer. *Climate Dyn.*, **45**, 1583–1599, https://doi.org/10.1007/s00382-014-2414-z.

——, ——, J. Zinke, and L. Harrison, 2017: Modulation of the southern Africa precipitation response to the El Niño–Southern Oscillation by the subtropical Indian Ocean Dipole. *Climate Dyn.*, **48**, 2529–2540, https://doi.org/10.1007/s00382-016-3220-6.

Hoskins, B. J., and D. J. Karoly, 1981: The steady linear response of a spherical atmosphere to thermal and orographic forcing. *J. Atmos. Sci.*, **38**, 1179–1196, https://doi.org/10.1175/1520-0469(1981)038<1179:TSLROA>2.0.CO;2.

——, and P. J. Valdes, 1990: On the existence of storm-tracks. *J. Atmos. Sci.*, **47**, 1854–1864, https://doi.org/10.1175/1520-0469(1990)047<1854:OTEOST>2.0.CO;2.

Kanamitsu, M., W. Ebisuzaki, J. Woollen, S. K. Yang, J. Hnilo, M. Fiorino, and G. L. Potter, 2002: NCEP–DOE AMIP II reanalysis (R-2). *Bull. Amer. Meteor. Soc.*, **83**, 1631–1643, https://doi.org/10.1175/BAMS-83-11-1631.

Knippertz, P., 2007: Tropical-extratropical interactions related to upper-level troughs at low latitudes. *Dyn. Atmos. Oceans*, **43**, 36–62, https://doi.org/10.1016/j.dynatmoce.2006.06.003.

Landman, W. A., and S. J. Mason, 1999: Change in the association between Indian Ocean sea-surface temperatures and summer rainfall over South African and Namibia. *Int. J. Climatol.*, **19**, 1447–1492, https://doi.org/10.1002/(SICI)1097-0088(19991115)19:13<1477::AID-JOC432>3.0.CO;2-W.

Lee, H.-T., 2014: Climate algorithm theoretical basis document (C-ATBD): Outgoing longwave radiation (OLR)—Daily. Tech. Rep. CDRP-ATBD-0526, DSR-661, NOAA's Climate Data Record (CDR) Program, 46 pp., http://www1.ncdc.noaa.gov/pub/data/sds/cdr/CDRs/Outgoing%20Longwave%20Radiation%20-%20Daily/AlgorithmDescription.pdf.

Lenters, J. D., and K. H. Cook, 1997: On the origin of the Bolivian high and related circulation features of the South American climate. *J. Atmos. Sci.*, **54**, 656–677, https://doi.org/10.1175/1520-0469(1997)054<0656:OTOOTB>2.0.CO;2.

Liñán, C. C., 2008: *cvBlob*. Accessed 15 February 2018, https://code.google.com/archive/p/cvblob/.

Lindesay, J. A., 1988: South African rainfall, the Southern Oscillation and a Southern Hemisphere semi-annual cycle. *Int. J. Climatol.*, **8**, 17–30, https://doi.org/10.1002/joc.3370080103.

——, and M. R. Jury, 1991: Atmospheric circulation controls and characteristics of a flood event in central South Africa. *Int. J. Climatol.*, **11**, 609–627, https://doi.org/10.1002/joc.3370110604.

Macron, C., B. Pohl, Y. Richard, and M. Bessafi, 2014: How do tropical temperature troughs form and develop over southern Africa? *J. Climate*, **27**, 1633–1647, https://doi.org/10.1175/JCLI-D-13-00175.1.

Manhique, A., C. J. C. Reason, L. Rydberg, and N. Fauchereau, 2011: ENSO and Indian Ocean sea surface temperature and their relation with tropical temperate troughs over Mozambique and the Southwest Indian Ocean. *Int. J. Climatol.*, **31**, 1–13, https://doi.org/10.1002/joc.2050.

Mason, S. J., 1995: Sea-surface temperature—South African rainfall associations, 1910–1989. *Int. J. Climatol.*, **15**, 119–135, https://doi.org/10.1002/joc.3370150202.

Nicholson, S. E., and J. Kim, 1997: The relationship of the El-Niño-Southern Oscillation to African rainfall. *Int. J. Climatol.*, **17**, 117–135, https://doi.org/10.1002/(SICI)1097-0088(199702)17:2<117::AID-JOC84>3.0.CO;2-O.

Nogues-Paegle, J., and K. C. Mo, 1997: Alternating wet and dry conditions over South America during summer. *Mon. Wea. Rev.*, **125**, 279–291, https://doi.org/10.1175/1520-0493(1997)125<0279:AWADCO>2.0.CO;2.

Puaud, Y., B. Pohl, N. Fauchereau, C. Macron, and G. Beltrando, 2017: Climate co-variability between South America and Southern Africa at interannual, intraseasonal and synoptic scales. *Climate Dyn.*, **48**, 4029–4050, https://doi.org/10.1007/s00382-016-3318-x.

Rasmusson, E. M., and T. H. Carpenter, 1982: Variations in tropical sea surface temperature and surface wind fields associated with the Southern Oscillation/El Niño. *Mon. Wea. Rev.*, **110**, 354–384, https://doi.org/10.1175/1520-0493(1982)110<0354:VITSST>2.0.CO;2.

Ratna, S. B., S. Behera, J. V. Ratnam, K. Takahashi, and T. Yamagata, 2013: An index for tropical temperate troughs over southern Africa. *Climate Dyn.*, **41**, 421–441, https://doi.org/10.1007/s00382-012-1540-8.

Ratnam, J. V., S. K. Behera, Y. Masumoto, and T. Yamagata, 2014: Remote effects of El Niño and Modoki events and the austral summer precipitation of southern Africa. *J. Climate*, **27**, 3802–3815, https://doi.org/10.1175/JCLI-D-13-00431.1.

——, Y. Morioka, S. K. Behera, and T. Yamagata, 2015: A model study of regional air-sea interaction in the austral summer precipitation over southern Africa. *J. Geophys. Res. Atmos.*, **120**, 2342–2357, https://doi.org/10.1002/2014JD022154.

Reason, C. J. C., 2001: Subtropical Indian Ocean SST dipole events and southern African rainfall. *Geophys. Res. Lett.*, **28**, 2225–2227, https://doi.org/10.1029/2000GL012735.

——, 2002: Sensitivity of the southern African circulation to dipole SST patterns in the South Indian Ocean. *Int. J. Climatol.*, **22**, 377–393, https://doi.org/10.1002/joc.744.

——, 2016: The Bolivian, Botswana, and Bilybara Highs and Southern Hemisphere drought/floods. *Geophys. Res. Lett.*, **43**, 1280–1286, https://doi.org/10.1002/2015GL067228.

——, and H. Mulenga, 1999: Relationships between South African rainfall and SST anomalies in the southwest Indian Ocean. *Int. J. Climatol.*, **19**, 1651–1673, https://doi.org/10.1002/(SICI)1097-0088(199912)19:15<1651::AID-JOC439>3.0.CO;2-U.

——, and D. Jagadheesha, 2005: A model investigation of recent ENSO impacts over southern Africa. *Meteor. Atmos. Phys.*, **89**, 181–205, https://doi.org/10.1007/s00703-005-0128-9.

——, R. J. Allan, J. A. Lindesay, and T. J. Ansell, 2000: ENSO and climatic signals across the Indian Ocean Basin in the global context: Part I, interannual composite patterns. *Int. J. Climatol.*, **20**, 1285–1327, https://doi.org/10.1002/1097-0088(200009)20:11<1285::AID-JOC536>3.0.CO;2-R.

Reynolds, R. W., N. A. Rayner, T. M. S. D. Stokes, and W. Wang, 2002: An improved in situ and satellite SST analysis for climate. *J. Climate*, **15**, 1609–1625, https://doi.org/10.1175/1520-0442(2002)015<1609:AIISAS>2.0.CO;2.

Richard, Y., S. Trzaska, P. Roucou, and M. Rouault, 2000: Modification of the southern African rainfall variability/ENSO relationship since the late 1960s. *Climate Dyn.*, **16**, 883–895, https://doi.org/10.1007/s003820000086.

Rouault, M., P. Florenchie, N. Fauchereau, and C. J. C. Reason, 2003: South East tropical Atlantic warm events and southern African rainfall. *Geophys. Res. Lett.*, **30**, 8009, https://doi.org/10.1029/2002GL014840.

Sardeshmukh, P. D., and B. J. Hoskins, 1988: The generation of global rotational flow by steady idealized tropical divergence. *J. Atmos. Sci.*, **45**, 1228–1251, https://doi.org/10.1175/1520-0469(1988)045<1228:TGOGRF>2.0.CO;2.

Schwendike, J., P. Govekar, M. J. Reeder, R. Wardle, G. J. Berry, and C. Jakob, 2014: Local partitioning of the overturning circulation in the tropics and the connection to the Hadley and Walker circulations. *J. Geophys. Res. Atmos.*, **119**, 1322–1339, https://doi.org/10.1002/2013JD020742.

Streten, N., 1973: Some characteristics of satellite-observed bands of persistent cloudiness over the Southern Hemisphere. *Mon. Wea. Rev.*, **101**, 486–495, https://doi.org/10.1175/1520-0493(1973)101<0486:SCOSBO>2.3.CO;2.

Todd, M., and R. Washington, 1999: Circulation anomalies associated with tropical-temperate troughs in Southern Africa and the south west Indian Ocean. *Climate Dyn.*, **15**, 937–951, https://doi.org/10.1007/s003820050323.

Tyson, P. D., 1986: *Climatic Change and Variability in Southern Africa*. Oxford University Press, 220 pp.

Tziperman, E., L. Stone, M. A. Cane, and H. Jarosh, 1994: El Niño chaos: Overlapping of resonances between the seasonal cycle and the Pacific ocean-atmosphere oscillator. *Science*, **264**, 72–74, https://doi.org/10.1126/science.264.5155.72.

Usman, M. T., and C. J. C. Reason, 2004: Dry spell frequencies and their variability over southern Africa. *Climate Res.*, **26**, 199–211, https://doi.org/10.3354/cr026199.

van der Walt, S., J. L. Schönberger, J. Nunez-Iglesias, F. Boulogne, J. D. Warner, N. Yager, E. Gouillart, and T. Yu, 2014: scikit-image: Image processing in Python. *PeerJ*, **2**, e453, https://doi.org/10.7717/peerj.453.

van der Wiel, K., A. J. Matthews, D. P. Stevens, and M. M. Joshi, 2015: A dynamical framework for the origin of the diagonal South Pacific and South Atlantic convergence zones. *Quart. J. Roy. Meteor. Soc.*, **141**, 1997–2010, https://doi.org/10.1002/qj.2508.

Ventura, V., C. J. Paciorek, and J. S. Risbey, 2004: Controlling the proportion of falsely rejected hypotheses when conducting multiple tests with climatological data. *J. Climate*, **17**, 4343–4356, https://doi.org/10.1175/3199.1.

Washington, R., and A. Preston, 2006: Extreme wet years over southern Africa: Role of Indian Ocean sea surface temperatures. *J. Geophys. Res.*, **111**, D15104, https://doi.org/10.1029/2005JD006724.

Wilks, D. S., 2016: ''The stippling shows statistically significant grid points'': How research results are routinely overstated and overinterpreted, and what to do about it. *Bull. Amer. Meteor. Soc.*, **97**, 2263–2273, https://doi.org/10.1175/BAMS-D-15-00267.1.

Yu, J.-Y., C. Chou, and J. D. Neelin, 1998: Estimating the gross moist stability of the tropical atmosphere. *J. Atmos. Sci.*, **55**, 1354–1372, https://doi.org/10.1175/1520-0469(1998)055<1354:ETGMSO>2.0.CO;2.